Supplementary Information

Scalable, Low-Cost Ink-Based Processing of High-Performance Silver Selenide Thermoelectrics

Md. Omarsany Bappy[a, b], Guoyue Xu[a], Kaidong Song[a], Qiang Jiang[a], Paribesh Acharyya[c], Berardo Matalucci[d], Allen Gray[d], Mercouri Kanatzidis[c], Tengfei Luo[a], and Yanliang Zhang*[a]

[a]*Department of Aerospace and Mechanical Engineering, University of Notre Dame, Notre Dame, IN 46556, USA*

[b]*Department of Mechanical Engineering, Bangladesh University of Engineering and Technology, Dhaka, 1000, Bangladesh*

[c]*Department of Chemistry, Northwestern University, Evanston, IL 60208, USA*

[d]*MIMiC Systems, Brooklyn, NY 11205, USA*

**Email: yzhang45@nd.edu*

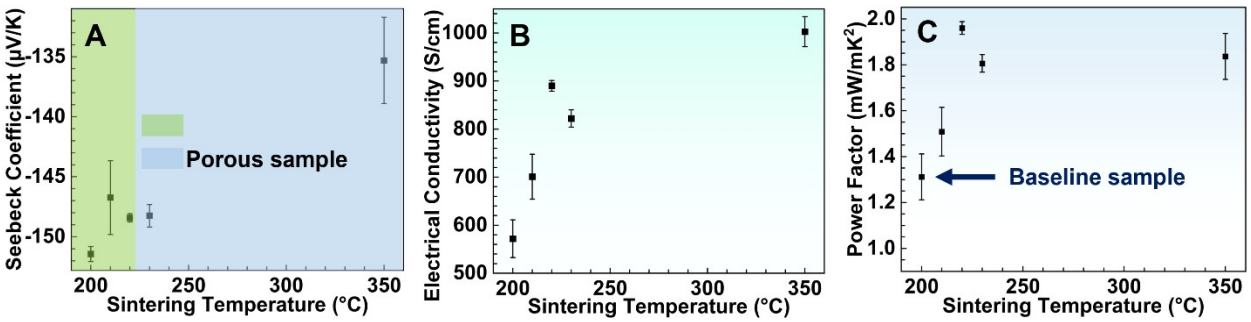

Figure S1. Thermoelectric properties: A) Seebeck coefficient, B) electrical conductivity, and C) power factor of silver selenide samples synthesized and sintered together at different temperatures.

Synthesis and sintering play a critical role in the performance of thermoelectric materials. Followed by blade-coating, drying, and cold pressing, the thermoelectric films are synthesized and sintered together at different temperatures inspired by the literature. The synthesis and sintering are done in a tube furnace for one hour in a forming gas environment. The samples sintered at 220 °C showed the highest power factor of 1.96 mW/m.K^2. Samples sintered at 350 °C showed the highest electrical conductivity of 1003 S/cm, the lowest Seebeck coefficient of -135.4 μV/K, with a power factor of 1.84 mW/m.K^2. The lowest Seebeck coefficient is due to the loss of selenium at temperatures higher than the melting point of selenium (220.8 °C). The samples sintered higher than the melting point of selenium were porous due to the evaporation and loss of selenium. The baseline samples were defined as those samples synthesized and sintered together at 200 °C.

Figure S2. Flow chart showing the silver selenide thermoelectric film fabrication process.

In a typical ink-based processing, the samples are synthesized and sintered together after cold-pressing. Here, to address the issue of porosity in the samples sintered at temperatures higher than the melting point of selenium, we separated the process. We are synthesizing the ink first, then cold-pressing and finally sintering the samples. We optimized both the synthesis and sintering conditions.

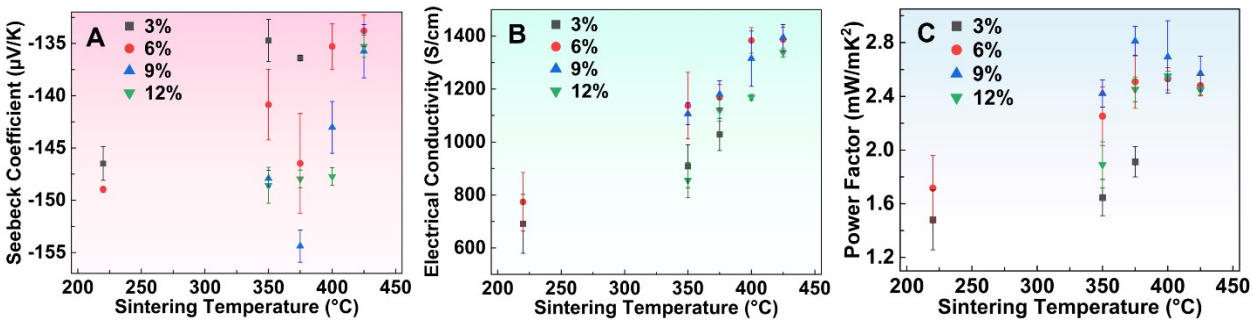

Figure S3. Optimization of excess selenium and sintering temperature. Extra selenium (wt.%) and sintering temperature dependent A) Seebeck coefficient, B) electrical conductivity, and C) power factor.

Here, the samples were synthesized at 350 °C for 90 minutes before cold-pressing and sintering. Samples with 9% excess selenium and sintered at 375 °C showed the highest power factor of 2.8 mW/m.K^2.

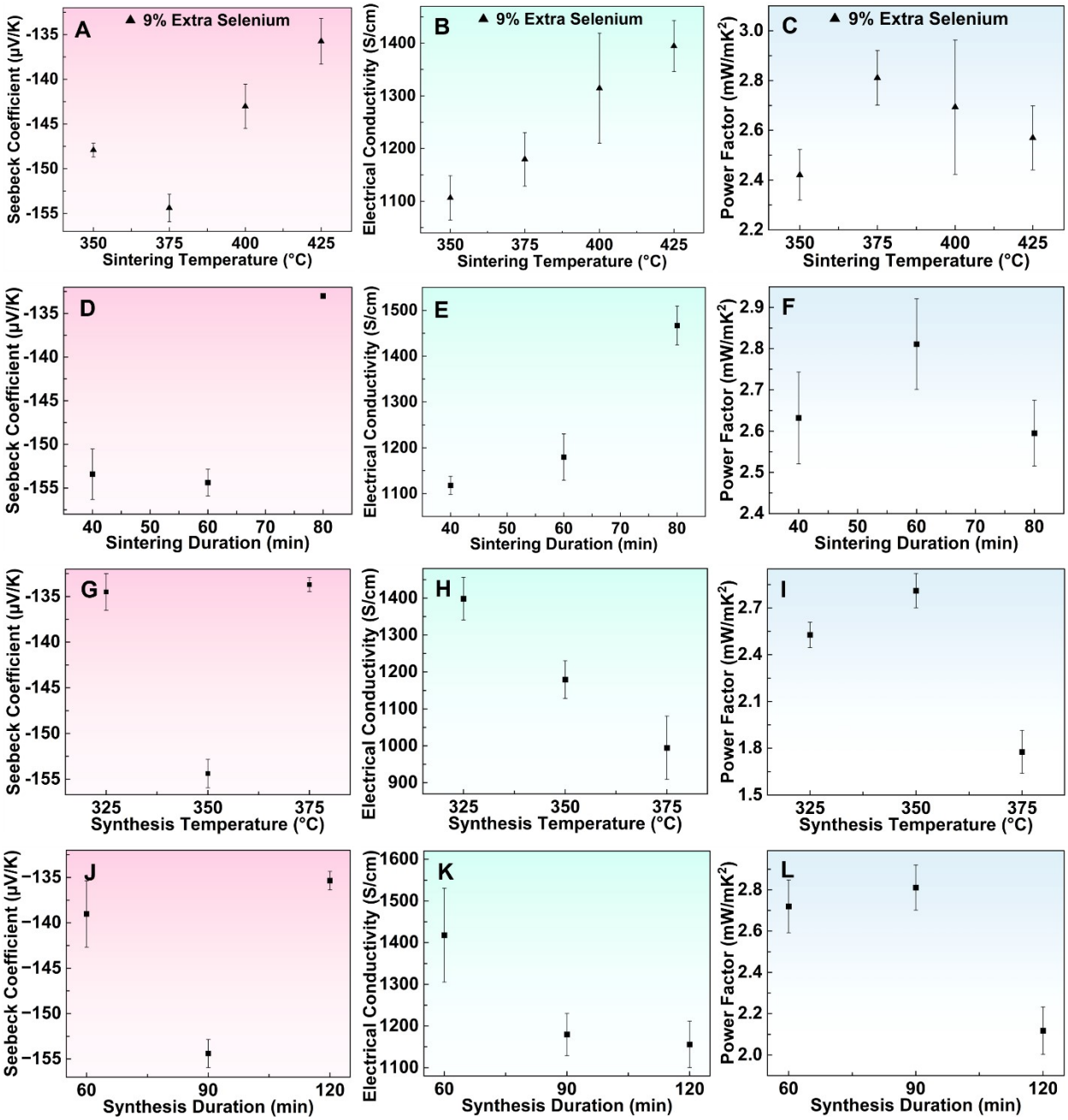

Figure S4. Optimization of sintering temperature A-C, sintering duration D-F, synthesis temperature G-I, and synthesis duration J-L.

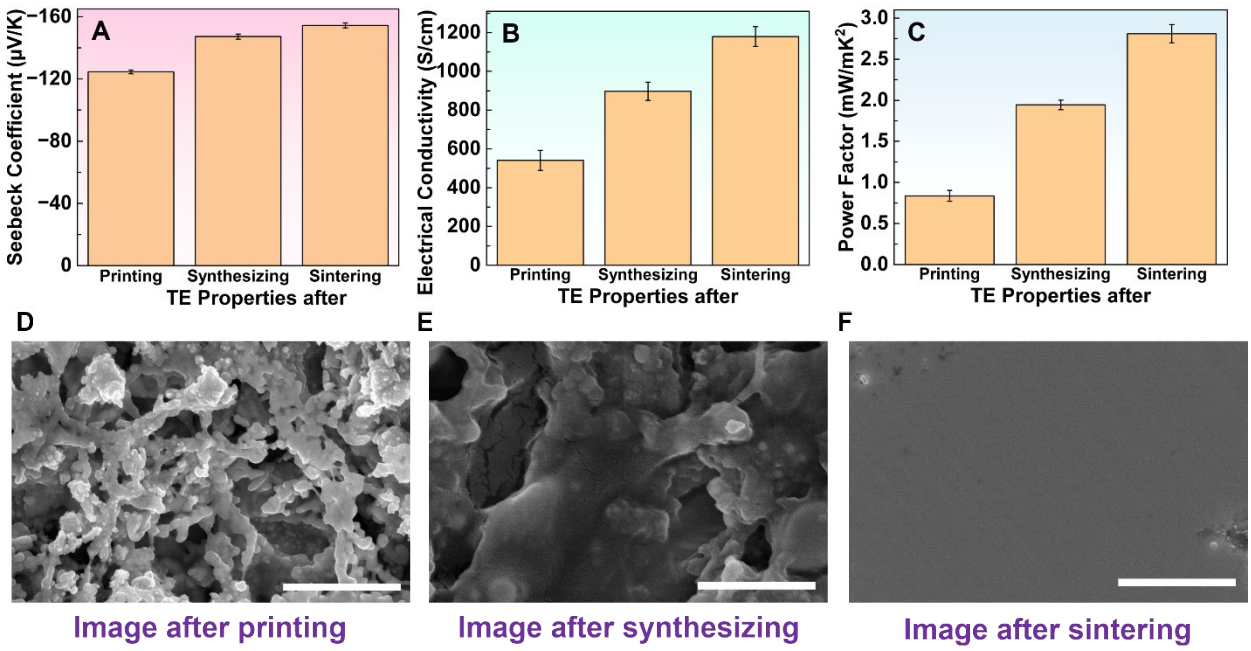

Figure S5. Thermoelectric properties of the silver selenide sample in between fabrication steps: A) Seebeck coefficient, B) electrical conductivity, and C) power factor. SEM images of the samples in between fabrication steps: D) after printing, drying, and cold-pressing, E) after synthesizing at 350 °C for 90 minutes, and F) after sintering at 375 °C for 60 minutes. Scale bar 1 μm.

To understand the impact of each fabrication step, we measured the thermoelectric (TE) properties of the optimized samples after printing, synthesizing, and sintering. After printing, we dried (100 °C for 6 hours in vacuum), cold-pressed (25 MPa for 10 minutes) the samples, and then measured the TE properties. The Seebeck coefficient at this stage is -124.5 μV/K, which confirms the spontaneous reaction between silver and selenium during the powder mixing and drying steps. As the samples are not sintered yet at high temperature, the electrical conductivity is 540.7 S/cm, and the microstructure at this stage shows significant porosities (Figure S5D). After synthesizing at 350 °C for 90 minutes, the samples show a significantly higher Seebeck coefficient of -147.26 μV/K, with an electrical conductivity of 897.6 S/cm as the reaction between Ag and Se proceeds toward the synthesis of AgSe alloy, with improved phase purity, increased density and reduced porosity, which lead to a consequent increase of both the Seebeck coefficient and electrical conductivity. The microstructure at this stage also shows well connected structure with certain porosity (Figure S5E). Finally, the sintering is done after cold-pressing the synthesized samples, and in this stage, the microstructure (Figure S5F) shows a very well-connected network with reduced porosities. This densification significantly reduces carrier scattering at particle interfaces and grain boundaries, improving carrier mobility and thus increasing electrical conductivity. These samples show the highest Seebeck coefficient (-154.4 μV/K), electrical conductivity (1179.6 S/cm), and power factor (2.81 mW/mK^2).

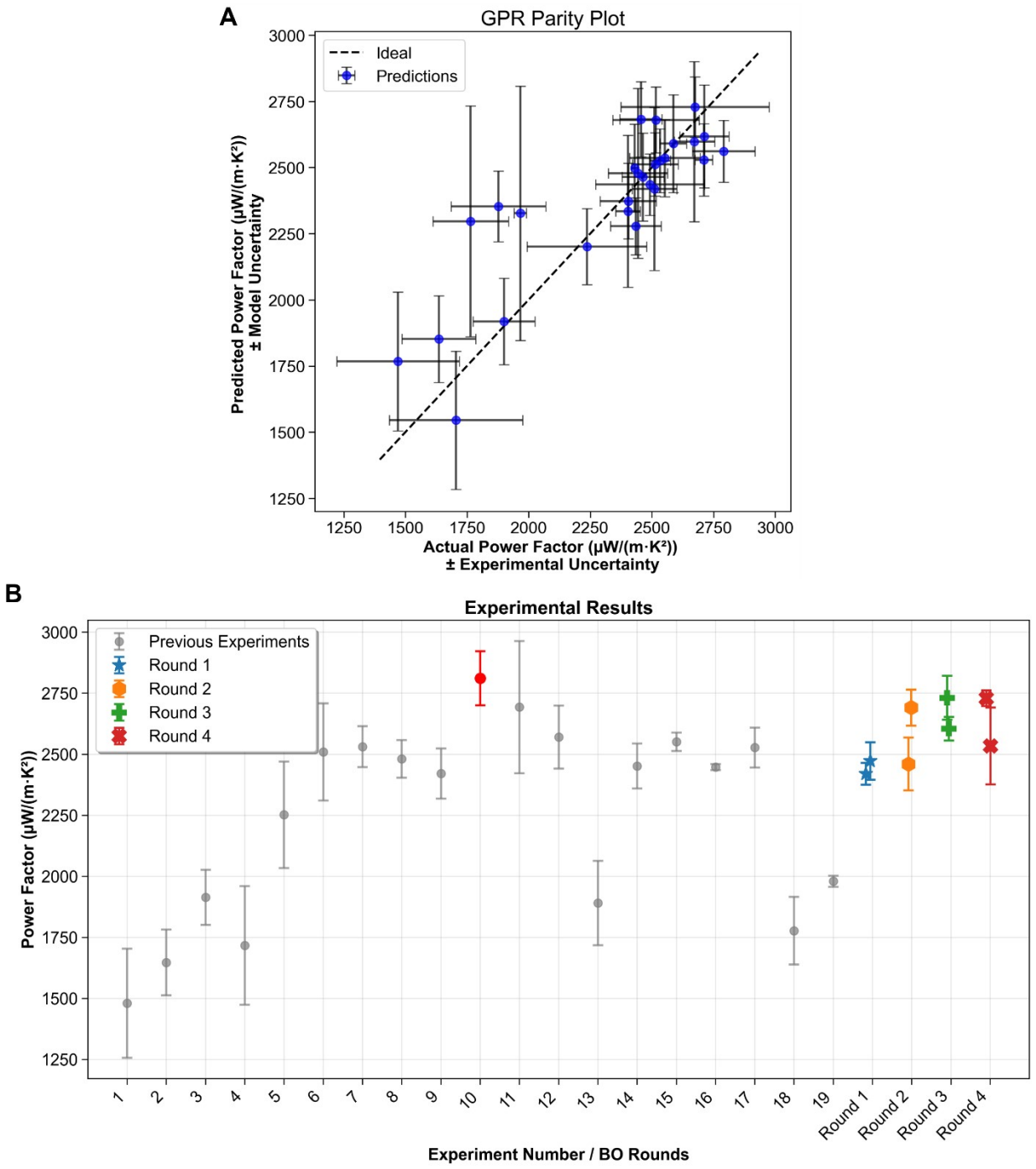

Figure S6. Model validation and experimental results. A) Parity plot comparing predicted and measured thermoelectric power factors. Vertical error bars represent the model-predicted uncertainty from the Gaussian Process Regression model, while horizontal error bars represent the experimental uncertainty obtained from repeated measurements. The ideal 1:1 line indicates perfect prediction. The model captures the overall trend of the data, yielding R^2= 0.711. B) Measured power factors in the dataset and across sequential Bayesian optimization rounds. Each color corresponds to one optimization round.

Table S1. Training data collection for the Bayesian optimization of the silver selenide samples. Each experiment contains at least 4 samples.

Exp. no.	Extra Selenium (% wt.)	Synthesis Temperature (°C)	Sintering Temperature (°C)	Electrical Conductivity (S/cm)	Seebeck Coefficient (μV/K)	Power Factor (mW/mK^2)
1	0.03	350	220	690±111	-146.5±1.6	1.48±0.22
2	0.03	350	350	908±81	-134.7±2.0	1.65±0.13
3	0.03	350	375	1028.6±60.7	-136.4±0.3	1.91±0.11
4	0.06	350	220	773.9±110.2	-149.0±0.3	1.72±0.24
5	0.06	350	350	1137.6±125.5	-140.9±3.4	2.25±0.22
6	0.06	350	375	1168.4±48.9	-146.5±4.8	2.51±0.20
7	0.06	350	400	1383.3±48.0	-135.3±2.1	2.53±0.08
8	0.06	350	425	1386.3±47.0	-133.8±1.5	2.48±0.07
9	0.09	350	350	1106.4±42.1	-147.9±0.8	2.42±0.10
10	0.09	350	375	1179.9±50.8	-154.4±1.5	2.81±0.11
11	0.09	350	400	1314.5±104.3	-143.0±2.5	2.69±0.27
12	0.09	350	425	1394.6±48.6	-135.8±2.5	2.57±0.13
13	0.12	350	350	855.7±66.4	-148.6±1.7	1.89±0.17
14	0.12	350	375	1120.3±41.2	-147.9±0.9	2.45±0.09
15	0.12	350	400	1168.9±10.8	-147.7±0.8	2.55±0.04
16	0.12	350	425	1337.8±17.0	-135.3±1.1	2.45±0.01
17	0.09	325	375	1398.0±57.9	-134.5±2.0	2.53±0.08
18	0.09	375	375	994.9±85.9	-133.7±0.8	1.78±0.14
19	0.2	300	450	957.4±92.5	-143.8±0.9	1.98±0.02

Table S2. Machine Learning (ML) guided optimization of silver selenide thermoelectric samples. Each batch contains at least 4 samples.

Round no.	Batch no.	Extra Selenium (% wt.)	Synthesis Temperature (°C)	Sintering Temperature (°C)	ML Predicted Power Factor (mW/mK^2)	Experimental Power Factor (mW/mK^2)
1	1	0.086	335	383	2.63±0.21	2.42±0.05
	2	0.086	344	383	2.78±0.15	2.47±0.077
2	3	0.044	318	450	2.34±0.42	2.69±0.074
	4	0.095	318	450	2.36±0.40	2.46±0.11
3	5	0.03	310	398	2.49±0.37	2.73±0.09
	6	0.05	310	398	2.48±0.36	2.60±0.05
4	7	0.03	306	450	2.60±0.31	2.73±0.03
	8	0.04	306	440	2.58±0.29	2.53±0.16

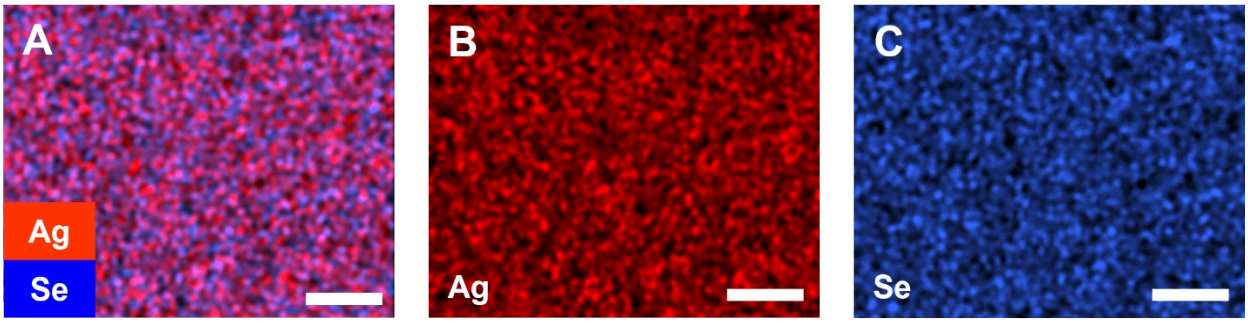

Figure S7. Energy dispersive X-ray spectrometry (EDS) elemental mapping of the optimized silver selenide sample (polished cross-section, corresponding to Fig. 2D). Scale bar 1 µm.

EDS elemental mapping was performed along the polished cross-section of the optimized sample to verify the elemental homogeneity. The obtained mapping results confirmed a uniform spatial distribution of all constituent elements throughout the sample, indicating successful synthesis and compositional uniformity without noticeable phase segregation or elemental clustering.

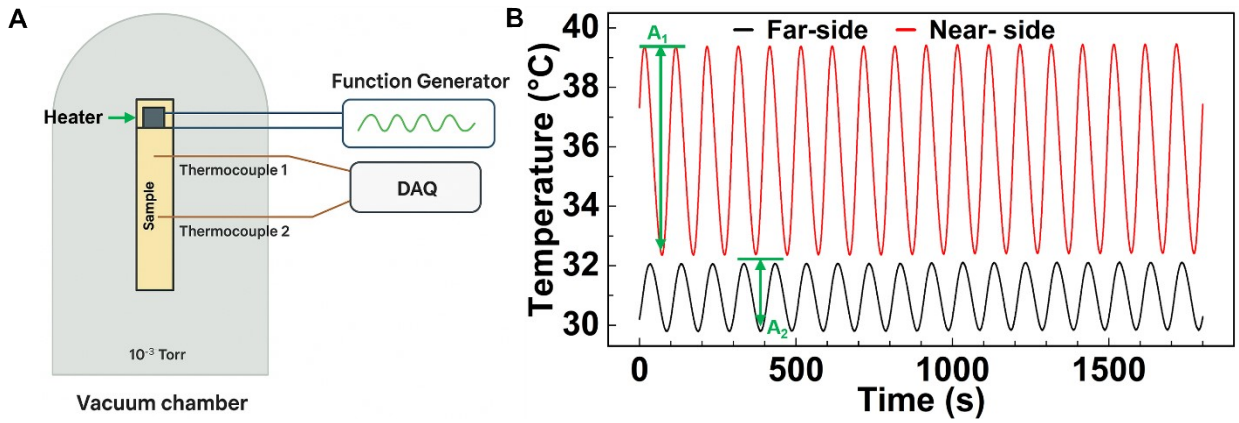

Figure S8. A) Schematic illustration of thermal diffusivity measurement by the Angstrom method. B) The sinusoidal temperature–time profile to determine the amplitude and phase difference between the two temperature signals, which are essential for evaluating the thermal diffusivity.

The in-plane thermal diffusivity of the optimized silver selenide sample was determined using the Angstrom method.[1] During the measurement, a function generator (RIGOL DG4062) supplied a periodic heat input to one end of the film under a vacuum environment (~2 mTorr). The resulting temperature oscillations were monitored at two distinct positions along the sample using a data acquisition system (Keysight 34970A), which captured both the amplitude and phase of the temperature response. Temperature measurements were recorded with two commercial K-type thermocouples (Omega, 5TC 40 AWG); one positioned near the heat source and the other placed at a known distance away. The excitation frequency was carefully chosen such that the thermal penetration depth was sufficiently large to produce measurable oscillations at the distant thermocouple, yet smaller than the spacing between the two thermocouples to maintain accurate phase resolution. The thermal diffusivity (α) was then calculated using the following relation:

$$\alpha = \frac{L^2}{2dtln\frac{A_1}{A_2}}$$

Here, A_1 and A_2 represent the temperature phase difference and amplitude at the near and far thermocouple positions, respectively, while L denotes the spacing between them. The thermal conductivity (κ) was derived from the measured thermal diffusivity (α) using the relation $\kappa = \alpha.\rho.c_p$, where ρ is the density and c_p is the specific heat capacity.

To validate the accuracy of the Angstrom method, the thermal diffusivity of fused quartz, mica, and high-density polyethylene (HDPE) materials with well-established reference values was also measured, as mentioned in the author's previous work.[2, 3] The obtained results exhibited excellent agreement with literature data, showing deviations of less than 5%. Although determining the thermal conductivity of thin films remains challenging, the Angstrom technique provides a reliable and widely accepted approach for characterizing diverse materials, including thermoelectric films.[4-7]

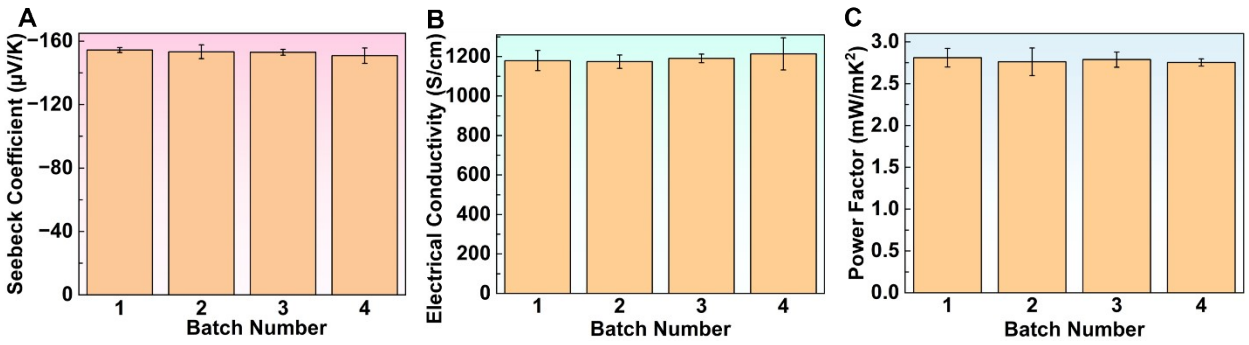

Figure S9. Batch-to-batch thermoelectric properties of A) Seebeck coefficient, B) electrical conductivity, and C) power factor.

To assess the reproducibility, we prepared four batches of samples (each batch containing at least four samples) under the sample conditions and measured their thermoelectric properties.

Table S3. Reproducibility of the blade-coated silver selenide thermoelectric samples (9 %wt. excess selenium, synthesis temperature 350 °C for 90 minutes, sintering temperature 375 °C for 60 minutes).

Batch no.	Sample no.	Electrical Conductivity, σ (S/cm)	Avg. σ (S/cm)	Seebeck Coefficient, S (μV/K)	Avg. S (μV/K)	Power Factor, PF (mW/mK²)	Avg. PF (mW/mK²)
1	1	1249	1180 ±51	-152.2	-154.4 ±1.5	2.89	2.81 ±0.11
	2	1183		-154.8		2.84	
	3	1106		-154.0		2.62	
	4	1180		-156.5		2.89	
2	1	1137	1174 ±34	-148.9	-153.3 ±4.4	2.52	2.76 ±0.17
	2	1152		-160.6		2.97	
	3	1182		-151.4		2.71	
	4	1226		-152.3		2.84	
3	1	1221	1191 ±22	-152.6	-153.0 ±1.8	2.84	2.79 ±0.09
	2	1180		-155.5		2.85	
	3	1200		-153.5		2.83	
	4	1163		-150.4		2.63	
4	1	1115	1214 ±81	-157.5	-150.9 ±4.8	2.76	2.76 ±0.04
	2	1310		-144.6		2.74	
	3	1276		-148.5		2.82	
	4	1154		-152.9		2.70	

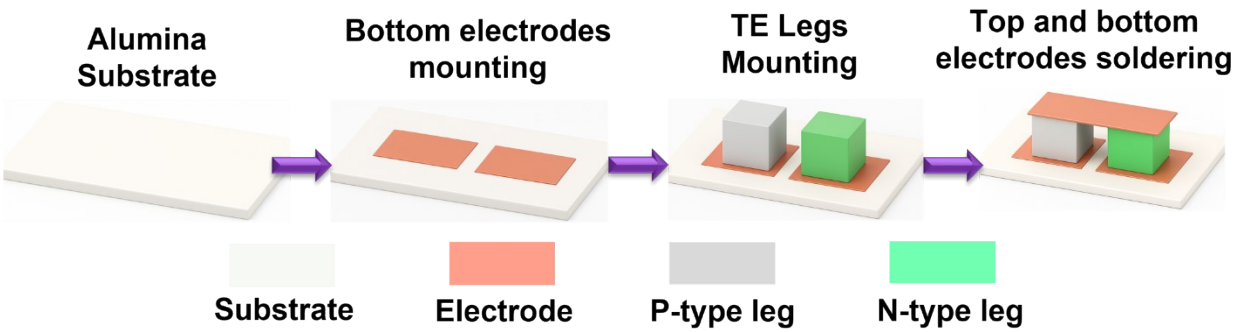

Figure S10. Schematic illustration of the step-by-step fabrication process of the cross-plane thermoelectric device.

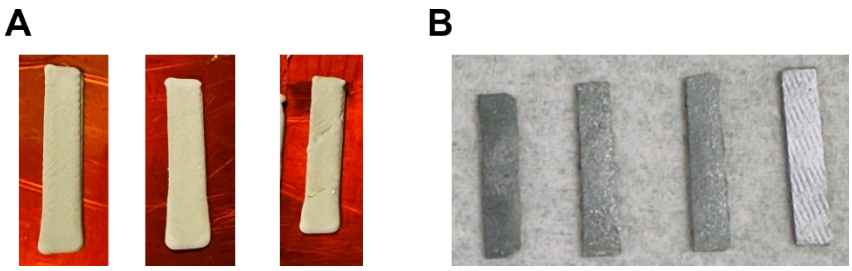

Figure S11. Images of the fabricated thermoelectric film. A) Image after blade-coating the sample on Kapton polyimide. B) Samples after drying, synthesizing, cold-pressing, and sintering.

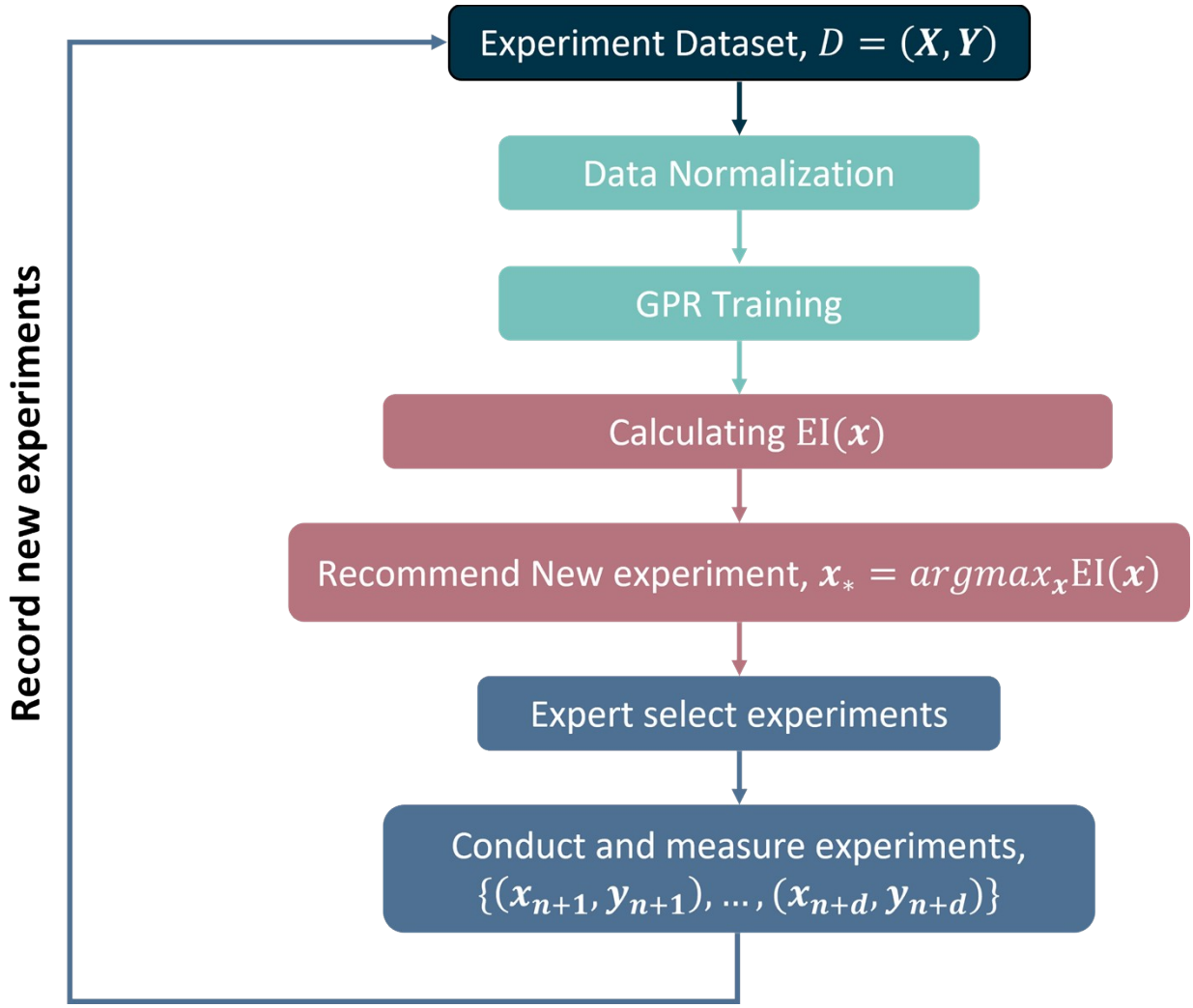

Figure S12. Workflow of the Gaussian Process-based BO loop. The process begins with an experimental dataset D = (X, Y) followed by data normalization and GPR training. The EI function is then calculated to identify promising candidates, and the point that maximizes EI is recommended for the next experiment. An expert reviews these recommendations before new experiments are conducted. Finally, the latest data is added to the dataset, and the loop repeats, allowing the model to refine its predictions and guide the next round.

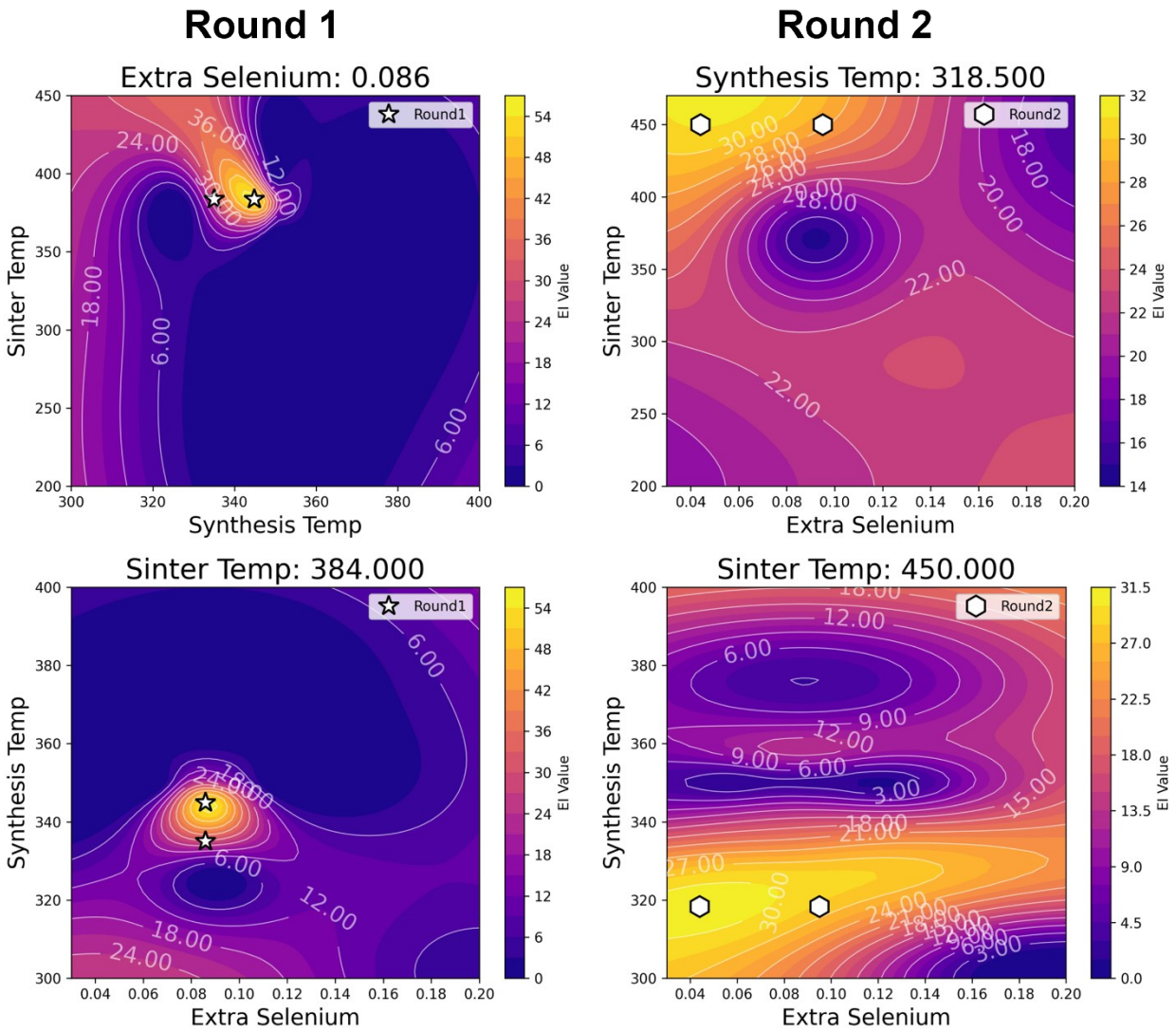

Figure S13. EI maps from the first two rounds of Bayesian optimization.

Contour plots show the EI values as a function of synthesis temperature, sintering temperature, and excess selenium. Each panel represents one optimization round. Brighter regions highlight where the model predicts the most significant performance gains. The star for Round 1 and the hexagon for Round 2 symbols marks the conditions chosen for the following experiments.

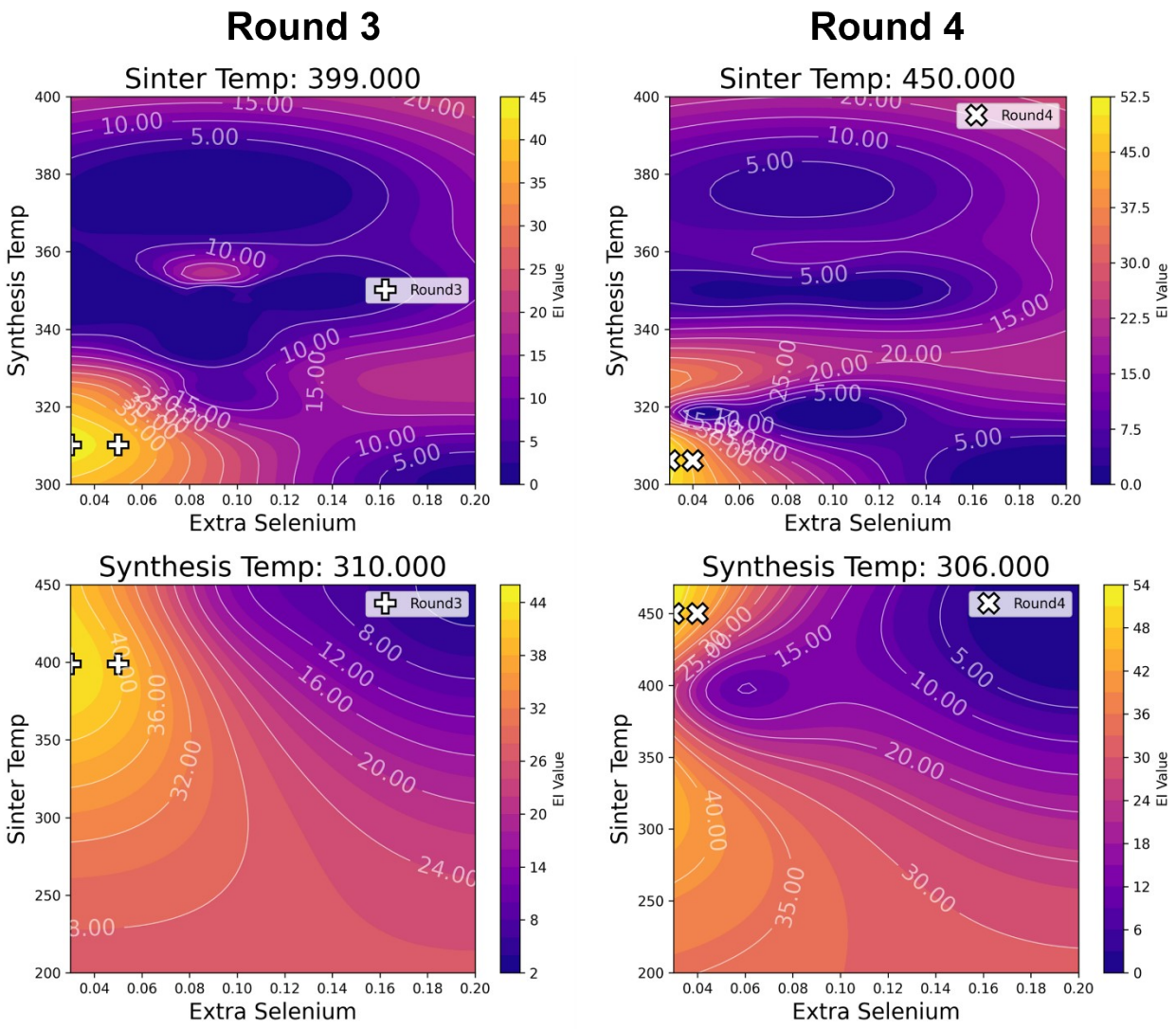

Figure S14. EI maps in round 3 and 4 of Bayesian optimization.

As the model incorporates more data, its understanding of the parameter space evolves. The plus pinpoints the chosen experimental parameters for Round 3, and the crossed circle symbolize Round 4.

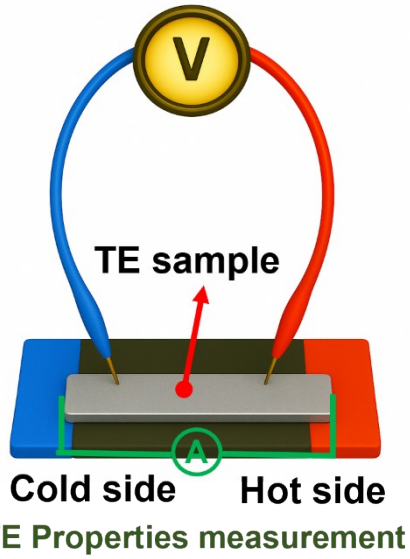

Figure S15. Schematic illustration of the Seebeck coefficient and electrical conductivity measurement setup of the free-standing thermoelectric film.

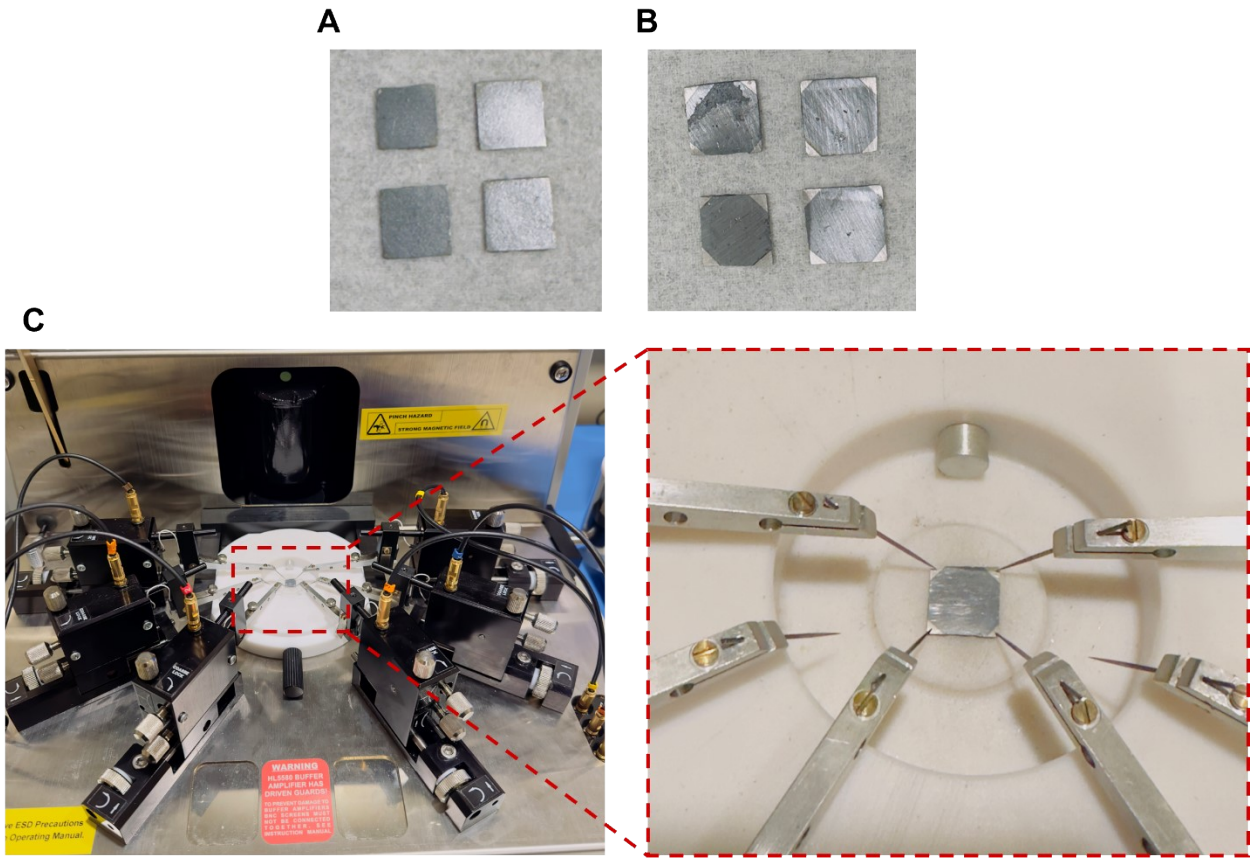

Figure S16. Images of the Hall effect measurement samples. A) Samples with the corners sputter-coated (30 nm Au/Pd alloy, 80% Au and 20% Pd). The color of the coated material and the silver selenide sample color are almost the same, so the differences are not visible that much. B) Samples with the corners sputter-coated (30 Iridium). C) Image showing the Hall effect measurement using the HL5500PC Hall effect system.

We tried two different types of sputter-coated material to reduce the contact resistance between the probe and the sample during the measurement. Both contact materials worked well.

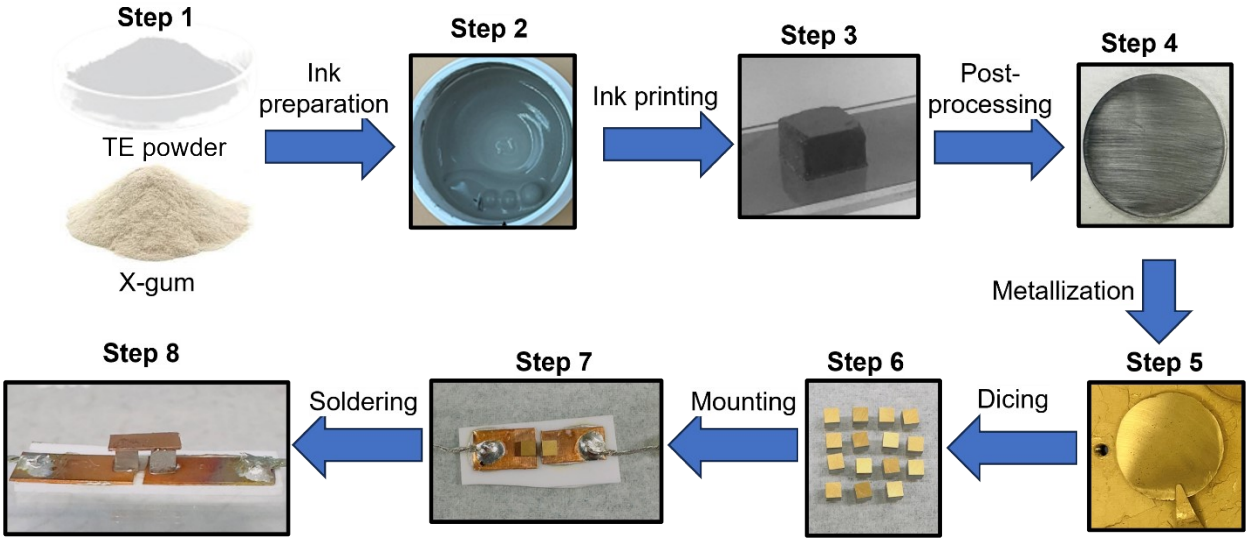

Figure S17. Steps of the 3D thermoelectric device fabrication process from silver and selenium particles.

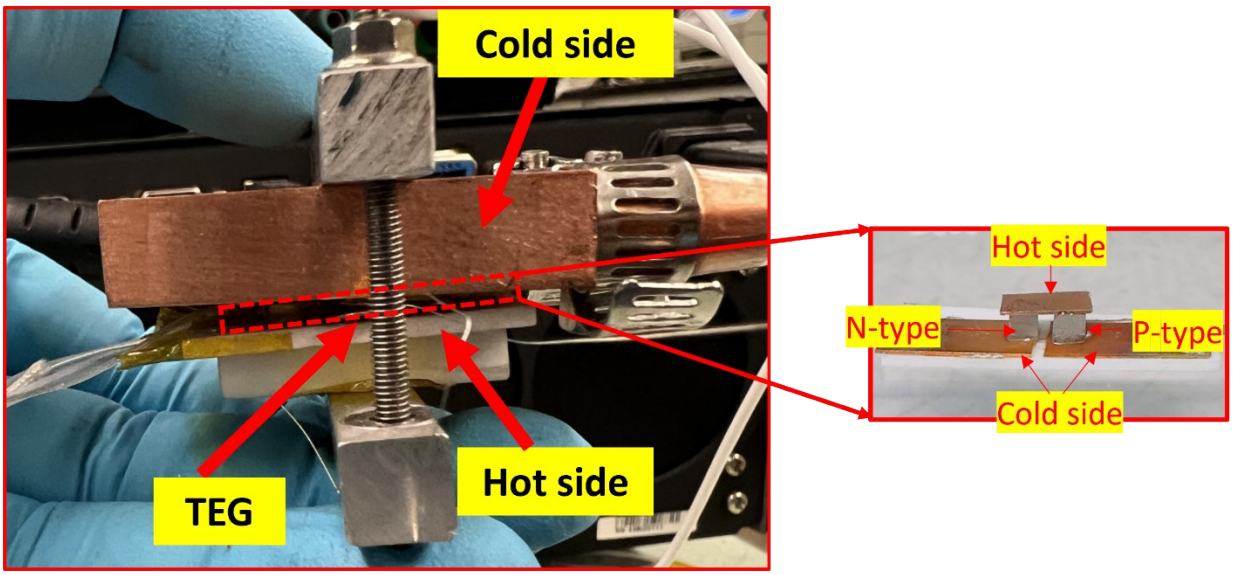

Figure S18. Custom-built experimental setup for the thermoelectric generator testing.

A resistive-based electric heater is used at the hot side of the TEG. The heater voltage is adjusted to control the hot side temperature. To maintain the cold side temperature as low as possible, we used a copper cold plate connected to a chiller (Precision Temperature Control System, ThermoTek). The chiller temperature is adjusted to control the cold side temperature of the TEG.

References

1. P. Kosky, D. Maylotte and J. Gallo, *International communications in heat and mass transfer*, 1999, **26**, 1051-1059.
2. K. Song, G. Xu, A. N. M. Tanvir, K. Wang, M. O. Bappy, H. Yang, W. Shang, L. Zhou, A. W. Dowling and T. Luo, *Journal of Materials Chemistry A*, 2024, **12**, 21243-21251.
3. A. N. M. Tanvir, M. O. Bappy, M. Zeng, W. Shang, K. Wang, K. Song, Y. Liu, E. Isotta, M. G. Kanatzidis and G. J. Snyder, *Energy & Environmental Science*, 2024, **17**, 4560-4568.
4. M. Saeidi-Javash, K. Wang, M. Zeng, T. Luo, A. W. Dowling and Y. Zhang, *Energy & Environmental Science*, 2022, **15**, 5093-5104.
5. F. Kim, B. Kwon, Y. Eom, J. E. Lee, S. Park, S. Jo, S. H. Park, B.-S. Kim, H. J. Im and M. H. Lee, *Nature Energy*, 2018, **3**, 301-309.
6. T. Varghese, C. Dun, N. Kempf, M. Saeidi-Javash, C. Karthik, J. Richardson, C. Hollar, D. Estrada and Y. Zhang, *Advanced Functional Materials*, 2020, **30**, 1905796.
7. J. Huang, R. B. Ambade, J. Lombardo, B. Brooks, A. Poosapati, P. Banerjee, M. Saeidi-Javash, Y. Zhang and D. Madan, *Applied Materials Today*, 2024, **37**, 102116.